SIMULATION OF LIDAR RETURN SIGNALS ASSOCIATED WITH WATER CLOUDS

A Thesis

by

JIANXU LU

Submitted to the Office of Graduate Studies of
Texas A&M University
in partial fulfillment of the requirements for the degree of

MASTER OF SCIENCE

August 2009

Major Subject: Atmospheric Sciences

SIMULATION OF LIDAR RETURN SIGNALS ASSOCIATED WITH WATER CLOUDS

A Thesis

by

JIANXU LU

Submitted to the Office of Graduate Studies of
Texas A&M University
in partial fulfillment of the requirements for the degree of

MASTER OF SCIENCE

Approved by:

Co-Chairs of Committee,	Ping Yang
	Sarah D. Brooks
Committee Members,	George W. Kattawar
	Chia-Ren Hu
Head of Department,	Kenneth P. Bowman

August 2009

Major Subject: Atmospheric Sciences

ABSTRACT

Simulation of Lidar Return Signals Associated with Water Clouds. (August 2009)

Jianxu Lu, B.S., University of Science and Technology of China;

M.S., Texas A&M University

Chair of Advisory Committee: Dr. Ping Yang

We revisited an empirical relationship between the integrated volume depolarization ratio, δ_{acc}, and the effective multiple scattering factor, $\bar{\eta}$, on the basis of Monte Carlo simulations of spaceborne lidar backscatter associated with homogeneous water clouds. The relationship is found to be sensitive to the extinction coefficient and to the particle size. The layer integrated attenuated backscatter is also obtained. Comparisons made between the simulations and statistics derived relationships of the layer integrated depolarization ratio, δ_{acc}, and the layer integrated attenuated backscatter, $\bar{\eta}$, based on the measurement by the Cloud-Aerosol Lidar and Infrared Pathfinder Satellite Observations (CALIPSO) satellite show that a cloud with a large effective size or a large extinction coefficient has a relatively large integrated backscatter and a cloud with a small effective size or a large extinction coefficient has a large integrated volume depolarization ratio. The present results also show that optically thin water clouds may not obey the empirical relationship derived by Y. X. Hu. and co-authors.

To those who failed and never get over it

ACKNOWLEDGMENTS

I would like to thank Dr. Ping Yang for suggesting this research and for his support in the past 20 months. Also I would like to thank the co-chair of my advisory committee, Dr. Sarah Brooks, and committee members, Dr. George Kattawar and Dr. Chia-Ren Hu.

Lastly, my appreciation goes to Dr. Pengwang Zhai, Dr. Yu You, Dr. Shouguo Ding, Dr. Gang Hong, Mr. Feng Zhang, Mr. Lei Bi, and Mr. Zhaokai Meng, for their help with my research.

TABLE OF CONTENTS

LIST OF FIGURES

FIGURE Page

FIGURE Page

CHAPTER I

INTRODUCTION

A. Background

The radiative transfer equation is not related to quantum mechanics. However, sometimes the term "photon" is borrowed to explain the process of transfer of light in a turbid medium, particularly in the case of Monte-Carlo simulation of the transfer of radiation [1]. These photons are scattered by particles in the medium again and again before they leave the medium or get absorbed by the medium. After each scattering event, the corresponding photon will be scattered in a particular direction. The view is very different in terms of a wave, the energy of a scattered light wave will be spread over all the directions, i.e. 4π steradian. In either instance, if we set up a detector (receiver) and a source (transmitter), the photons or light wave received by the detector might have been scattered more than one time after leaving the source. For such cases, the single-scattering lidar equation, very likely, can not be used to estimate the energy received by the detector. After interacting with the medium, the returning light wave carries some information from the medium. A good understanding of the multiple-scattering process and a good estimation of the energy of the returning light will help to correctly analyze the medium and to retrieve the information. For this reason we are interested in the multiple-scattering lidar equation.

The journal model is *Applied Optics*.

Clouds are one of the most interesting turbid media. As clouds float above us everyday, they play important roles in our lives. They reflect solar radiation during the day to keep the earth's temperature down and absorb the earth's infrared energy at night to keep the atmosphere warm. Clouds are very important regulators of the earth's energy budget. Their influence on us depends on their altitude, phase, optical thickness, extinction coefficient and effective particle size. Scientists have been conducting research on these influences using many methods of which lidar is one.

Experimental and theoretical research on lidar-backscatters from clouds began about 40 years ago. A comprehensive introduction of some of the researche is given in section 3.2.2 of "Elastic Lidar " by Kovalev and Eichinger [2]. The single-scattering lidar equation can be found in Collis's work [3]. Later, the polarization related double scattering effect was studied by Liou and Schotland [4] and Eloranta [5]. A comparison between the experimental results and simulated double scattering results [6] showed large differences at a penetration depth greater than 70 meters. The effects of high order scattering has been studied by many researchers [7, 8, 9, 10, 11, 12, 13, 14, 15], and some of the multiple scattering lidar models developed were reviewed by Bissonnette et al. [16]. Sometimes, the simulated results from these models are quite different from each other under the same conditions and it is currently difficult to give an accurate interpretation of all the experimental measurements by using one physical model. However, it is concluded that the contribution of multiple scattering can not be ignored and can yield some properties like cloud phase [17] and particle size. One of the missions of the CALIPSO lidar is to measure the optical and physical

properties of clouds.

Among the attempted interpretations for experimental measurements, the simulated results achieved by Raković et al. [18, 19], showed a good agreement with the backscatter from suspended polystyrene spheres in deionized water and other measurements [20, 21, 22, 23]. Another attempt in which we are interested is the empirical relationship between multiple scattering and depolarization ratio derived from a Monte Carlo simulation of a ray tracing model [25, 26, 27]. Hu et al. [27] claimed that the relationship can be verified by the CALIPSO lidar measurements of opaque water clouds. However, the attempt was limited to the opaque water cloud and no explicit multiple-scattering lidar equation was obtained by Hu et al. Nevertheless, the relationship between simulated attenuated-backscatter and layer-integrated depolarization is not shown and the sensitivity studies on the empirical relationship are not very clear. Thus more details are needed for further research.

This thesis will present another way to derive the multiple-scattering lidar equation reported by Raković et al [19], and give an explanation of the Monte Carlo method used by Hu et al. [25]. Also, we will present the sensitivity analysis and a point of view of the CALIPSO lidar measurements of water clouds, which is different from that by Hu et al. We ignored the effect of atmospheric molecules and only considered a parallel plane cloud. The source and the detector are on the same satellite, which is 700 kms above the cloud.

In the remainder of this chapter, we will introduce some basic concepts that will be used in this thesis. In chapter two, we will present the physical model, and in chapter three, we will show the Monte-Carlo integration and model results. Chapter

four is the conclusion and a suggestion of future work.

B. Specific Intensity

The monochromatic radiant energy dE_λ is obtained as follows [28]:

$$d^4E_\lambda = I_{\lambda,specific} \cos\Theta d\omega d\lambda dt d\Sigma, \tag{1.1}$$

where $I_{\lambda,specific}$, Θ, $d\omega$, λ, and t are monochromatic specific intensity, the angle between the normal of area $d\Sigma$ and the direction of specific intensity $I_{\lambda,specific}$, the solid angle subtended by a light source element far away with the origin at $d\Sigma$, wavelength and time, respectively. As shown in Fig. 1, let the the area of a light source element be $d\sigma$, the angle between its normal and the direction of $I_{\lambda,specific}$ be ϑ, the distance between source and detector be r and:

$$I_{specific} = \int I_{\lambda,specific} d\lambda, \tag{1.2}$$

$$P_{ower} = \frac{dE}{dt}. \tag{1.3}$$

Then we obtain:

$$d\omega = \frac{d\sigma \cos\vartheta}{r^2}, \tag{1.4}$$

$$d^2P_{ower} = I_{specific} \frac{d\sigma \cos\vartheta}{r^2} d\Sigma \cos\Theta, \tag{1.5}$$

where Eq. (1.5) means the power received by the area element $d\Sigma$ is proportional to the specific intensity $I_{specific}$, the projection area of the light source, the projection area of the receiver and the inverse of r^2.

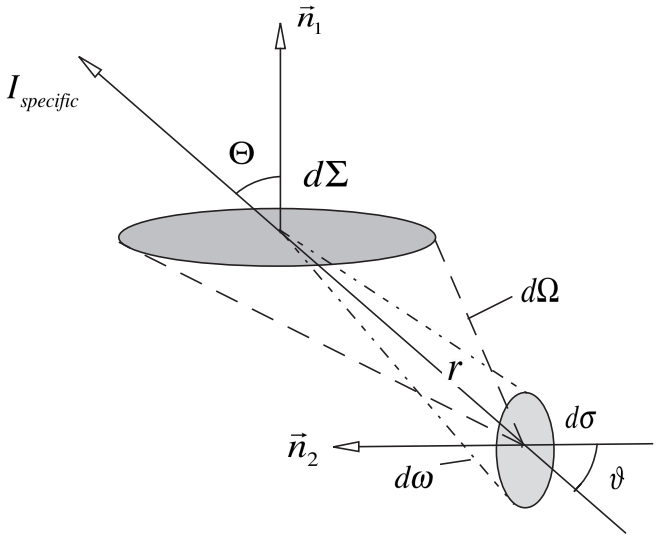

Fig. 1. Power transmitted through two surface elements. The figure is drawn following Chandrasekhar [28].

C. Stokes Parameter and Mueller Matrix of Particle System with Spherical Symmetry

The Stokes parameters used in this thesis are defined as follows:

$$I = \frac{1}{2}\epsilon_0 c(E_l^* E_l + E_r E_r), \tag{1.6}$$

$$Q = \frac{1}{2}\epsilon_0 c(E_l^* E_l - E_r E_r), \tag{1.7}$$

$$U = \frac{1}{2}\epsilon_0 c(E_l^* E_r + E_l E_r^*), \tag{1.8}$$

$$V = \frac{i}{2}\epsilon_0 c(E_l^* E_r - E_l E_r^*), \tag{1.9}$$

where E, c and ϵ_0 are the electric field, the speed of light and the permittivity in vacuum, respectively. l and r denote parallel and perpendicular components,

respectively. Different from the definition in many books, which are in Gaussian units, we chose multiply a factor of $\frac{1}{2}\epsilon_0 c$ to make the unit of I be $watt/m^2$. The factor $\frac{1}{2}$ denotes a time-averaged value. The unit of I is consistent with the unit of specific intensity introduced previously, because "steradian" is not a physical unit but a ratio. The ratio is important because r and $d\sigma$ usually can not be measured separately.

Let $(\vartheta_{in}, \varphi_{in})$ and lidar backscatter $(\vartheta_{sc}, \varphi_{sc})$ denote the directions of the incident ray and the scattered ray, respectively. Then the angle θ between them can be obtained by a dot product:

$$\cos\theta = \cos\vartheta_{in}\cos\vartheta_{sc} + \sin\vartheta_{in}\sin\vartheta_{sc}\cos(\varphi_{in} - \varphi_{sc}), \tag{1.10}$$

where in and sc stand for incident ray and scattered ray, respectively. For water droplets or any particles with spherical symmetry, the relationship between the Stoke parameters of the incident ray and the scattered ray in far-field can be expressed in

terms of θ [29]:

$$\begin{pmatrix} I \\ Q \\ U \\ V \end{pmatrix}_{sc} = \frac{\sigma_s}{4\pi r^2} P(\theta) \begin{pmatrix} I \\ Q \\ U \\ V \end{pmatrix}_{in}, \tag{1.11}$$

$$P(\theta) = \begin{pmatrix} P_{11} & P_{12} & 0 & 0 \\ P_{12} & P_{22} & 0 & 0 \\ 0 & 0 & P_{33} & P_{34} \\ 0 & 0 & -P_{34} & P_{44} \end{pmatrix}, \tag{1.12}$$

where σ_s is the scattering (s) cross section of the scatterer, a quantity defined for the conservation of energy scattered. An absorption cross section, σ_a, is defined for energy absorbed and an extinction cross section, $\sigma_e$is defined:

$$\sigma_e = \sigma_a + \sigma_s. \tag{1.13}$$

The Stokes parameters of incident and scattered ray are referred to the scattering plane, which is determined by incident ray and scattered ray. However, sometimes we prefer Stokes parameters being referred to their own meridian plane as shown in Fig. 2 [28]. We write the Mueller matrix in terms of $(\vartheta_{in}, \varphi_{in}, \vartheta_{sc}, \varphi_{sc})$ [28]:

$$P(\vartheta_{in}, \varphi_{in}, \vartheta_{sc}, \varphi_{sc}) = L(-i_2))P(\Theta)L(-i_1), \tag{1.14}$$

where $L(\phi)$ is for rotation operator for Stoke parameter (I, Q, U, V) [30]:

$$L(\phi) = \begin{pmatrix} 1 & 0 & 0 & 0 \\ 0 & \cos 2\phi & \sin 2\phi & 0 \\ 0 & -\sin 2\phi & \cos 2\phi & 0 \\ 0 & 0 & 0 & 1 \end{pmatrix}. \tag{1.15}$$

where ϕ is an angle. i_1 is the angle between the meridian plane of incident ray and scattering plane while i_2 is the angle between the meridian plane of scattered ray and scattering plane:

$$\cos\vartheta_{sc} = \cos\theta_{sc}\cos\vartheta_{in} + \sin\theta_{sc}\sin\vartheta_{in}\cos(i_1), \tag{1.16}$$

$$\cos\vartheta_{in} = \cos\theta\cos\vartheta_{sc} + \sin\theta\sin\vartheta_{sc}\cos(i_2), \tag{1.17}$$

The rotation, $L(\phi)$, will be performed counter-clockwise from the meridian plane of incident ray to scattering plane and then from scattering plane to the meridian plane of scattered ray [31]. For the cases of water clouds, we obtain [32]:

$$P(\vartheta_{in}, \varphi_{in}, \vartheta_{SC}, \varphi_{SC}) = \begin{pmatrix} P_{11} & P_{12}C_1 & -P_{12}S_1 & 0 \\ P_{21}C_2 & P_{22}C_1C_2 - P_{33}S_1S_2 & -P_{22}S_1C_2 - P_{33}C_1S_2 & -P_{34}S_2 \\ P_{21}S_2 & P_{22}C_1S_2 + P_{33}S_1C_2 & -P_{22}S_1S_2 + P_{33}C_1C_2 & P_{34}C_2 \\ 0 & P_{43}S_1 & P_{43}C_1 & P_{44} \end{pmatrix}, \tag{1.18}$$

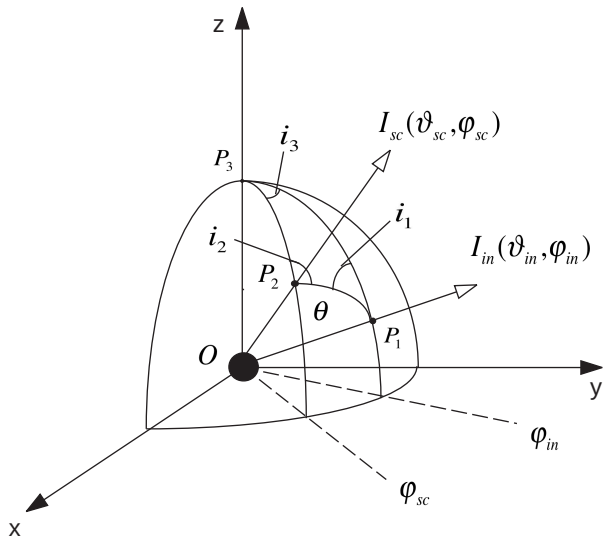

Fig. 2. Directions of the incident ray and the scattered ray in the same coordinate. The figure is drawn following Chandrasekhar [28].

where

$$C_1 = \cos 2i_1,\ S_1 = \sin 2i_1, \tag{1.19}$$

$$C_2 = \cos 2i_2,\ S_2 = \sin 2i_2. \tag{1.20}$$

For cases other than spherical particles, the phase matrix is:

$$P(\vartheta_{in}, \varphi_{in}, \vartheta_{sc}, \varphi_{sc}) = \begin{pmatrix} P_{11} & P_{12} & P_{13} & P_{14} \\ P_{21} & P_{22} & P_{23} & P_{24} \\ P_{31} & P_{32} & P_{33} & P_{34} \\ P_{41} & P_{42} & P_{43} & P_{44} \end{pmatrix}, \tag{1.21}$$

The technical details of calculating Mueller matrix, $P(\theta, \phi)$, is beyond the scope of this thesis, and may be found in van de Hulst [33].

D. Examples of Monte Carlo Integration

Multidimensional definite integrals are always involved with the multiple scattering problem. Because numerical methods for such integrals are extremely time consuming if we follow the usual algorithms which evaluate the integrand on a regular grid, randomly chosen points are used in the Monte Carlo integration. For convenience, we give an example of a one-dimensional-integral. For usual algorithms, we have

$$\int_a^b f(x)dx \simeq \sum_{i=1}^{i=N} f(x_i)\Delta x, \tag{1.22}$$

$$\Delta x = \frac{b-a}{N}, \tag{1.23}$$

$$x_i = a + (i - 1/2)\Delta x. \tag{1.24}$$

In the Monte Carlo integration, a series of randomly generated x_i' are used to replace x_i in Eq. (1.22)-(1.24). Assume ξ_i are random numbers between 0 and 1:

$$\int_a^b f(x)dx \simeq \sum_{i=1}^{i=N} f(x_i')\frac{b-a}{N}, \tag{1.25}$$

$$x_i' = a + (b-a)\xi_i. \tag{1.26}$$

To study multiple-scattering lidar returns, the following two integrals were frequently used and evaluated by the Monte-Carlo method [19]:

$$P_{cumu}(\theta) = \frac{1}{2}\int_0^\theta P_{11}(\theta)\sin\theta' d\theta' = -\frac{1}{2}\int_0^\theta P_{11}(\theta')d\cos\theta' = \int_0^{\theta'} dP_{cumu}(\theta'), \tag{1.27}$$

$$\text{with } \theta \in (0,\pi) \text{ and } P_{cumu}(\pi) = 1;$$

$$W(x) = \int_0^x e^{-x'}dx' = -\int_0^x de^{-x'} = 1 - e^{-x}, \tag{1.28}$$

$$\text{with } x \in (0,\infty) \text{ and } W(\infty) = 1.$$

$P_{cumu}(\theta)$ and $W(x)$ are sampled by two random number generators, then θ and x can be retrieved by using Eq. (1.27) and (1.28). When the Mueller matrix is involved,

importance sampling is adopted:

$$\begin{aligned}
&\int_0^{\theta} \begin{pmatrix} P_{11} & P_{12} & 0 & 0 \\ P_{21} & P_{22} & 0 & 0 \\ 0 & 0 & P_{33} & P_{34} \\ 0 & 0 & P_{43} & P_{44} \end{pmatrix} \sin\theta' d\theta' \\
= &\int_0^{\theta} \begin{pmatrix} 1 & P_{12}/P_{11} & 0 & 0 \\ P_{21}/P_{11} & P_{22}/P_{11} & 0 & 0 \\ 0 & 0 & P_{33}/P_{11} & P_{34}/P_{11} \\ 0 & 0 & P_{43}/P_{11} & P_{44}/P_{11} \end{pmatrix} dP_{cumu}(\theta').
\end{aligned} \tag{1.29}$$

Fig. 3 is an example of $P_{cumu}(\theta)$. Readers may refer to Weinzierl [34] for detailed discussions of Monte-Carlo Integration.

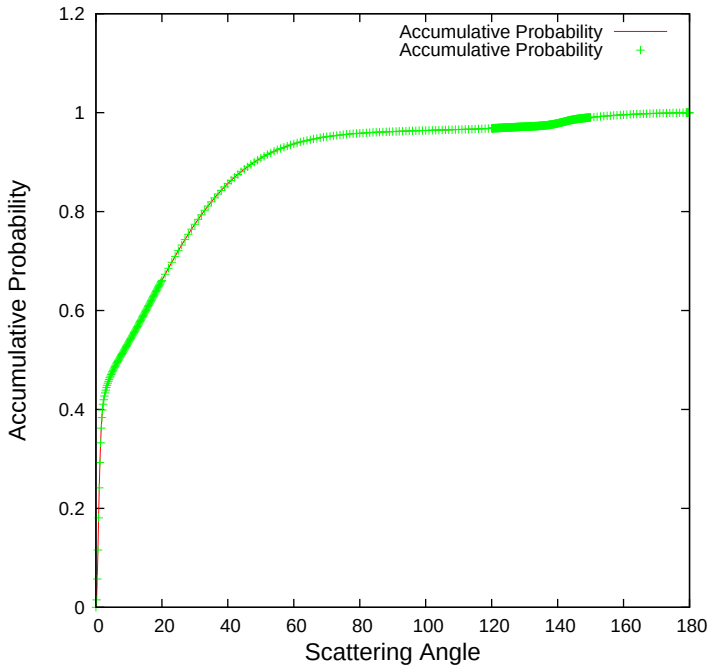

Fig. 3. Accumulative probability for a water cloud with $r_{eff} = 8.0\mu m$, $v_{eff} = 0.1$ and $\lambda = 0.532\mu m$.

CHAPTER II

PHYSICAL MODEL

A. The Multiple Scattering Lidar Equation

Although there have been a number of models developed in the past 40 years, we chose the physical model based on the works of Rakovi and Kattawar [18, 19] and Hu et al. [25]. In this section, we will derive the model in an easier and different way.

Fig. 4 shows the first three-order-scattering of a ray, which can be explained in terms of photon tracing. The terms I_n, m_n, r_n, and n represent the intensity, $(watt/m^2)$ the scattering position, the distance from m_{n-1} to m_n , and the order number, respectively. Two kinds of coordinate systems are involved, namely translational Cartesian coordinates (x'_n, y'_n, z'_n) and scattering Cartesian coordinates (x_n, y_n, z_n). When n is equal to 1 or 2, the two coordinates coincide, all the translational Cartesian coordinates, which are not shown, are parallel to each other with the origin moving from one scattering position to another. In the scattering Cartesian coordinate, z_n is always along I_{n-1}, and the plane $x_n m_{n-1} z_n$ coincides with the meridian plane of I_{n-1} in the translational Cartesian coordinate. As is well known, the transformation between these two coordinates can be performed by three properly chosen Euler angles and the matrixes performing these operations are unitary; thus,

$$dx_n dy_n dz_n = dx'_n dy'_n dz'_n. \tag{2.1}$$

Because the phase matrix is calculated in terms of the scattering angle in the scattering plane, we will use spherical coordinates:

$$x_n = r_n \sin\theta'_n \cos\phi'_n, \tag{2.2}$$

$$y_n = r_n \sin\theta'_n \sin\phi'_n, \tag{2.3}$$

$$z_n = r_n \cos\theta'_n, \tag{2.4}$$

$$x'_n = r_n \sin\vartheta'_n \cos\varphi'_n, \tag{2.5}$$

$$y'_n = r_n \sin\vartheta'_n \sin\varphi'_n, \tag{2.6}$$

$$z'_n = r_n \cos\vartheta'_n. \tag{2.7}$$

Let (ϑ_n, φ_n) and (θ_n, ϕ_n) be the directions of I_n in its own translational coordinate and its scattering coordinate, respectively. The relationship between (ϑ_n, φ_n) and (θ_n, ϕ_n) is known as:

$$\cos\theta_n = \cos\vartheta_n \cos\vartheta_{n-1} + \sin\vartheta_n \sin\vartheta_{n-1} \cos(\varphi_n - \varphi_{n-1}), \tag{2.8}$$

$$\cos\vartheta_n = \cos\theta_n \cos\vartheta_{n-1} + \sin\theta_n \sin\vartheta_{n-1} \cos(i_{1(n)}), \tag{2.9}$$

$$\cos\vartheta_{n-1} = \cos\theta_n \cos\vartheta_n + \sin\theta_n \sin\vartheta_n \cos(i_{2(n)}), \tag{2.10}$$

with the result:

$$i_{1(n)} = \phi_n. \tag{2.11}$$

$i_{1(n)}$ and $i_{2(n)}$ are the same as i_1 and i_2 mentioned previously.

Assuming the medium is macroscopically uniform, we can use the same phase

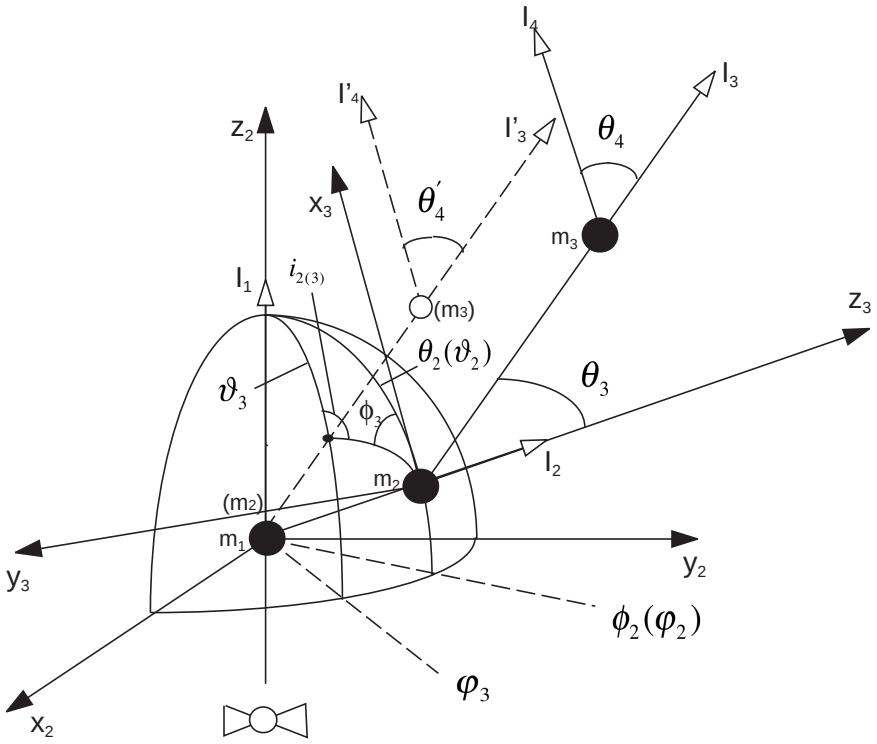

Fig. 4. Geometry of the first three order scatterings (flipped with the satellite at bottom). $\mathbf{I}'_3$, $\mathbf{I}'_4$ and θ'_4 are for $\mathbf{I}_3$, $\mathbf{I}_4$ and θ_4, respectively, when the origin of translational coordinate moves to m_2.

matrix at each scattering position. Microscopically, each position contains a number of small particles and has spherical symmetry, thus a Gamma distribution is needed. To understand these assumptions, some words from section 17 of [28] will be helpful:

> *"· · · we must first inquire how an element of volume containing a large number of particles, as distinct from a single particle, will scatter light. The question at issue here is whether the light scattered by different particles in a small element of volume can be considered independent or not. While a rigorous examination of this equation requires some careful consideration, it is nevertheless, fairly evident that if the scattering centres are distributed in a perfect random fashion (as in a gas obeying Maxwell's law) there would be no permanent correlations in the phases of light scattered by different particles. And if this is the case, the light scattered by the different particles will indeed be independent and we can add the Stokes parameters. · · · "*

Thus, Eq. (1.11) is not only good for calculating the far zone radiation of a single particle, but also can be used when a number of particles are present. The scattering cross section σ is not just for a single particle but for a number of particles included in a small volume dV:

$$\sigma = \beta_s dV = \beta_s r^2 \sin\theta dr d\theta d\phi, \tag{2.12}$$

where β_s is scattering coefficient, or in other words, the total scattering cross section per unit volume. Its relationships with extinction coefficient, β_e, absorption

coefficient, β_a, and single scattering albedo, ω_s are known as:

$$\beta_e = \beta_s + \beta_a, \tag{2.13}$$

$$\omega_s = \frac{\beta_s}{\beta_e}. \tag{2.14}$$

Thus we obtain:

$$\begin{pmatrix} dI \\ dQ \\ dU \\ dV \end{pmatrix}_{sc} = \frac{\beta_e \omega_s r_{in}^2 \sin\theta dr_{in} d\theta d\phi}{4\pi r_{sc}^2} P(\theta,\phi) \begin{pmatrix} I \\ Q \\ U \\ V \end{pmatrix}_{in}. \tag{2.15}$$

Instead of making r_{in} and r_{sc} equal in Eq. (2.15), r_{in} is the distance from the previous scattering cross section element. Since the Mueller matrix is defined by far field radiation, we should be cautious when we deal with a small r, which leads to a singularity in Eq. (2.15).

The dependence on $1/r^2$ can also be found in Eq. (2.15) as we did in Eq. (1.5). The similarity with Eq. (1.5) could be found when we define the projected area dS_1 and dS_2:

$$dS_1 = d\sigma \cos\vartheta, \tag{2.16}$$

$$dS_2 = d\Sigma \cos\Theta, \tag{2.17}$$

$$I' = \frac{dP_{ower}}{dS_2}, \tag{2.18}$$

then Eq. (1.5) becomes:

$$dI' = \frac{dS_1}{r^2} I_{specifc} \tag{2.19}$$

However, the scattered light in a medium will suffer attenuation due to more scatterings. The intensity of transmitted ray is approximated by the Beer-Bouguer-Lambert Law:

$$dI(r) = -\beta_e I(0) e^{-\beta_e r} dr = -\beta_e I(r) dr. \tag{2.20}$$

The scattered intensity between r and $r + dr$ is proportional to the extinction coefficient, β_e, the average intensity and the increment, dr. The scattered intensity, $dI(r)$, will spread over 4π steradian solid angle as described in Eq. (2.15). A combination of Eq. (2.15) and Eq. (2.20) gives:

$$\begin{pmatrix} dI_{n+1} \\ dQ_{n+1} \\ dU_{n+1} \\ dV_{n+1} \end{pmatrix}_{r_{n+1}} = \frac{e^{-\beta_e r_{n+1}} r_n^2 \sin\theta_n d\theta_n d\phi_n}{r_{n+1}^2} \frac{P(\theta_{n+1}, \phi_{n+1})}{4\pi} \begin{pmatrix} I_n \\ Q_n \\ U_n \\ V_n \end{pmatrix}_{r_n} \beta_e \omega_s dr_n \tag{2.21}$$

$$= \frac{\beta_e \omega_s dV_n}{r_{n+1}^2} \frac{P(\theta_{n+1}, \phi_{n+1})}{4\pi} \begin{pmatrix} I_n \\ Q_n \\ U_n \\ V_n \end{pmatrix}_{r_n} e^{-\beta_e r_{n+1}}. \tag{2.22}$$

Since $(\theta_{n+1}, \phi_{n+1})$ can be expressed in terms of $(\vartheta_{n+1}, \varphi_{n+1}, \vartheta_n, \varphi_n)$, Eq. (2.21)

can be written as:

$$\begin{pmatrix} dI_{n+1} \\ dQ_{n+1} \\ dU_{n+1} \\ dV_{n+1} \end{pmatrix}_{r_{n+1}} = \frac{\beta_e \omega_s dV_n}{r_{n+1}^2} \frac{P(\vartheta_{n+1}, \varphi_{n+1}, \vartheta_n, \varphi_n)}{4\pi} \begin{pmatrix} I_n \\ Q_n \\ U_n \\ V_n \end{pmatrix}_{r_n} e^{-\beta_e r_{n+1}}. \tag{2.23}$$

For convenience, let $\vec{I_n}$ denote (I_n, Q_n, U_n, V_n), then we obtain the mth order Stoke parameter:

$$\begin{aligned} \vec{I}_{m+1}(\vartheta_{m+1}, \varphi_{m+1}) = \frac{\beta_e^m \omega_s^m}{(4\pi)^m r_{m+1}^2} \int_m \cdots \int_1 \big(\prod_{n=2}^{n=m} P(\vartheta_{n+1}, \varphi_{n+1}, \vartheta_n, \varphi_n) \big) \\ \times P(\vartheta_2, \varphi_2, \vartheta_1, \varphi_1) e^{-\beta_e (\sum_{n=2}^{m+1} r_n)} \vec{I}_1 \big(\prod_{n=2}^{n=m} \frac{dV_n}{r_n^2} \big) dV_1. \end{aligned} \tag{2.24}$$

However, this is just a part of the contribution to the total power. As shown in Fig. 5, the power received at point E is a sum of the power of different scattering order from all directions. Assume the area of the receiver is A, and let γ_i $(i = 1, 2, 3, \cdots, N)$ denote the angles between the normal of A and the direction of those incoming intensities I^i, then we obtain:

$$P_{ower} = \sum_{i=1}^{N} I^i A \cos \gamma_i. \tag{2.25}$$

Because each Stokes parameter is referred to a certain plane through its direction of propagation, the sum, as we did in Eq. (2.25), can only be performed when all the Stokes parameters of incoming intensities are referred to the same plane. For convenience, this plane, in the translational coordinate defined previously, is chosen

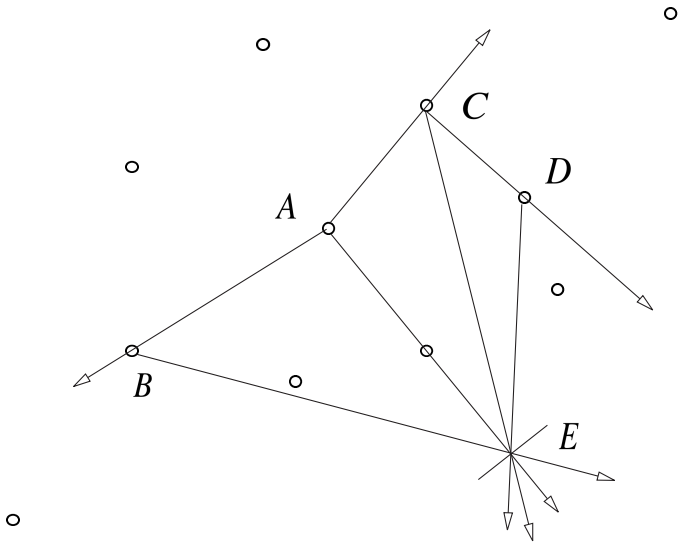

Fig. 5. A sketch of multiple scatterings.

to be a plane that is parallel to the plane $x_2 m_1 z_2$, which also is the reference plane of initial ray. A rotation $L(\phi)$, Eq. (1.15), should be performed on the incoming Stokes parameter, where ϕ is the angle rotated and we obtain:

$$\vec{I}_{tot} = \sum_{i=1}^{N} L(\phi^i)\vec{I}^i A \cos\gamma_i. \tag{2.26}$$

However, Eq. (2.26) is only good for a steady light source while we are dealing with a pulsed laser, emitting a pulse with pulse length 20 nsec and repetition rate 20.16 Hz. So energy (photons is not accurate but it is a convention) that arrives at the receiver at the same time should be summed. As we can see in Eq. (2.24) and Fig. 4, the path of each ray is uniquely recorded by a series of $(r_n, \vartheta_n, \varphi_n)$, thus the time used from leaving the laser to returning to the receiver can be calculated. Moreover,

the laser is stationed on a satellite, about 700 kms above the earth's surface, and has a field of view (FOV) of 130 μrad and a footprint of 100 μrad. We assume the angles γ_i, which are between directions of returning rays and the normal of the receiver, and the polar angle of initial ray to be zero.

$$\vartheta_1 = 0, \tag{2.27}$$

$$\vartheta_{m+1} = \pi, \tag{2.28}$$

which leads to:

$$\varphi_1 = \varphi_2, \tag{2.29}$$

$$\varphi_{m+1} = \varphi_m, \tag{2.30}$$

$$\varphi_2 = \phi_2 = i_{1(2)}, \tag{2.31}$$

$$\vartheta_2 = \theta_2, \tag{2.32}$$

$$\theta_{m+1} = \pi - \vartheta_m \tag{2.33}$$

As mentioned previously, Stokes parameters of emitted ray and returning ray are referred to the plane $x_2 m_1 z_2$, and we need a rotation matrix, $L(-\phi_i)$, for the emitted ray and another rotation matrix $L(-\phi_f)$ for the returning ray. Notice that when the returning ray is inverted, we obtain:

$$\phi_i = \varphi_2, \tag{2.34}$$

$$\phi_f = \varphi_{m+1}. \tag{2.35}$$

Assume there is a parallel plane cloud just above the earth's surface and there

is nothing else between the cloud and the satellite. Then only energy contributions from scattering events which happened in the cloud and in the FOV can be detected by the receiver:

$$0 < \sum_{n=1}^{n=m} z'_n < L, \tag{2.36}$$

$$\sqrt{(\sum_{n=1}^{n=m} x'_n)^2 + (\sum_{n=1}^{n=m} y'_n)^2} < \frac{700km \times 130\mu rad}{2}, \tag{2.37}$$

where L is the thickness of the cloud. Furthermore, if I_{m+1} is the intensity of the ray returning to the receiver, the optical depth, $\beta_e r_{m+1}$, should be modified by:

$$\tau_{bk} = \beta_e \Big| \sum_{n=1}^{m} z'_n(\vartheta_n, \varphi_n) \Big|, \tag{2.38}$$

where "bk" stands for coming back. Then for a single returning ray, we obtain:

$$\begin{aligned}
&\int_{d\Omega_{bk}} r_{bk}^2 d\Omega_{bk} L(-\phi_f) \vec{I}_{m+1} \\
&= \frac{\beta_s^m A}{(4\pi)^m r_{bk}^2} \int_m \dots \int_1 L(-\varphi_{m+1}) P(\vartheta_{m+1} = \pi, \varphi_{m+1} = \varphi_m, \vartheta_m, \varphi_m) \\
&\times \Big(\prod_{n=3}^{n=m} P(\vartheta_n, \varphi_n, \vartheta_{n-1}, \varphi_{n-1}) \Big) P(\vartheta_2, \varphi_2, \vartheta_1 = 0, \varphi_1 = \varphi_2) \\
&\times e^{-\tau_{bk} - \beta_e \sum_{n=2}^{m} r_n} L(-\varphi_1) \vec{I}_1 \Big(\prod_{n=2}^{n=m} \frac{dV_n}{r_n^2} \Big) dV_1
\end{aligned} \tag{2.39}$$

where $r_{bk} = r_{m+1} \simeq 700$ km. Symmetry can be found between emitted ray and returning ray in Eq. (2.39).

B. The Source Term

However, we haven't determined $\vec{I_1}$ yet. For convenience, we adopt a normalized delta function ray in a cylindrical coordinate. The intensity will be attenuated by cloud according to the Beer-Bouguer-Lambert Law:

$$\vec{I_1} = \vec{I_0} e^{-\beta_e z_1} = \begin{pmatrix} 1 \\ 1 \\ 0 \\ 0 \end{pmatrix} \frac{\delta(\rho_1)}{\pi \rho_1} e^{-\beta_e z_1}, \tag{2.40}$$

where (ρ_1, ϕ_1, z_1) are for the cylindrical coordinates and the Stokes parameter is referred to the plane $x_2 m_1 z_2$. We can use delta functions:

$$\vec{I_1} = \begin{pmatrix} 1 \\ 1 \\ 0 \\ 0 \end{pmatrix} \times \begin{cases} \frac{1}{\pi R^2} e^{-\beta_e z_1} & \text{if } 0 \le \rho_1 \le R \\ 0 & \text{if } \rho_1 > R \end{cases}; \tag{2.41}$$

or Gaussian distribution:

$$\vec{I_1} = \begin{pmatrix} 1 \\ 1 \\ 0 \\ 0 \end{pmatrix} \times \begin{cases} e^{-\rho_1^2/\alpha^2 - \beta_e z_1} / \left[\pi \alpha^2 (1 - e^{-R^2/\alpha^2})\right] & \text{if } 0 \le \rho_1 \le R \\ 0 & \text{if } \rho_1 > R \end{cases}; \tag{2.42}$$

or angle distribution in a spherical coordinate as Bissonnette [14]:

$$\vec{I_1} \simeq \begin{pmatrix} 1 \\ 1 \\ 0 \\ 0 \end{pmatrix} \times \begin{cases} e^{-\vartheta_1^2/\alpha^2-\beta_e r_1}/\left[\pi\alpha^2(1-e^{-\vartheta_0^2/\alpha^2})\right] & \text{if } 0 \le \vartheta_1 \le \vartheta_0 \ll 1 \\ 0 & \text{if } \vartheta_1 > \vartheta_0 \end{cases}, \quad (2.43)$$

where R and ϑ_0 are used to confine the range, which should be determined by the FOV; and α is a positive constant which is used to control the standard deviation of the Gaussian distribution. When the angle ϑ is small, the difference between z_1 and r_1 is very limited.

1. Reduction to 1st order and 2nd order

Thus for the case of a water cloud, we obtain:

$$\begin{aligned} &\int_{d\Omega_{bk}} r_{bk}^2 d\Omega_{bk} L(-\phi_f)\vec{I}_{m+1} \\ &\simeq \frac{\beta_s^m A}{(4\pi)^m r_{bk}^2} \int_m \cdots \int_1 L(-\varphi_{m+1})\Big(\prod_{n=3}^{n=m+1} L(-i_{2(n)})P(\theta_n)L(-i_{1(n)})\Big) \\ &\times P(\theta_2) e^{-\tau_{bk}-\beta_e(\sum_{n=2}^{m} r_n + z_1)} L(-\phi_2) \begin{pmatrix} 1 \\ 1 \\ 0 \\ 0 \end{pmatrix} \frac{\delta(\rho_1)}{\pi\rho_1} \Big(\prod_{n=2}^{n=m} \frac{dV_n}{r_n^2}\Big) dV_1, \end{aligned} \quad (2.44)$$

where we have changed $L(-i_{2(2)})P(\theta_2)L(-i_{1(2)})$ to $P(\theta_2)$. That is because $\vec{I_1}$ is always along z axis. In such cases, $i_{1(n)}$ and $i_{2(n)}$ are either 0 or π, which leads to $P(\theta_2)$.

The power contribution from $1st$ order scattering (single scattering) is :

$$\begin{aligned}
&\int_{d\Omega_{bk}} r_{bk}^2 d\Omega_{bk} L(-\phi_f)\vec{I}_2 \\
= &\int_{d\Omega_{bk}} r_{bk}^2 d\Omega_{bk} \int_{V_1} \beta_s dV_1 L(-\phi_f) L(-i_{2(2)}) \frac{P(\theta_2)L(-\phi_2)}{4\pi r_2^2} e^{-\beta_e \tau_{bk}} \vec{I}_0(\rho_1, \phi_1, z=0) e^{-\beta_e z_1} \\
= &\int_{d\Omega_2} L(-\phi_2) \frac{P(\theta_2)L(-\phi_2)}{4\pi} d\Omega_2 \int_{V_1} \begin{pmatrix} 1 \\ 1 \\ 0 \\ 0 \end{pmatrix} \frac{\delta(\rho_1)}{\pi\rho_1} e^{-2\beta_e z_1} \beta_s dV_1, \qquad (2.45)
\end{aligned}$$

where τ_{bk} is equal to $\beta_e z_1$ according to Eq. (2.38). Notice that $L(-\phi_2)P(\theta_2)L(-\phi_2)$ is similar to Eq. (1.18) and from the integral:

$$\int_0^{2\pi} \cos^2 2\phi_2 d\phi_2 = \pi, \qquad (2.46)$$

$$\int_0^{2\pi} \sin^2 2\phi_2 d\phi_2 = \pi, \qquad (2.47)$$

we obtain:

$$\begin{aligned}
&\int_{d\Omega_2} L(-\phi_2) \frac{P(\theta_2)L(-\phi_2)}{4\pi} d\Omega_2 \\
= &\frac{2\pi}{4\pi} \int_{d\theta_2} \begin{pmatrix} P_{11}(\theta) & 0 & 0 & 0 \\ 0 & \frac{1}{2}(P_{22}(\theta) - P_{33}(\theta)) & 0 & 0 \\ 0 & 0 & -\frac{1}{2}(P_{22}(\theta) - P_{33}(\theta)) & 0 \\ 0 & 0 & 0 & P_{44}(\theta) \end{pmatrix} d\theta_2 \\
\simeq &\frac{A}{4\pi r_{bk}^2} \begin{pmatrix} P_{11}(\pi) & 0 & 0 & 0 \\ 0 & P_{11}(\pi) & 0 & 0 \\ 0 & 0 & -P_{11}(\pi) & 0 \\ 0 & 0 & 0 & P_{44}(\pi) \end{pmatrix}. \qquad (2.48)
\end{aligned}$$

Then the power contribution from single scattering is:

$$\int_{d\Omega_{bk}} r_{bk}^2 d\Omega_{bk} L(-\phi_f)\vec{I}_2 = \int_{z_1} \frac{AP_{11}(\pi)}{4\pi r_{bk}^2} \begin{pmatrix} 1 \\ 1 \\ 0 \\ 0 \end{pmatrix} e^{-2\beta_e z_1} \beta_s dz_1. \qquad (2.49)$$

With the same method, the power contribution from doubly scattering is:

$$\begin{aligned}
&\int_{d\Omega_{bk}} r_{bk}^2 d\Omega_{bk} L(-\phi_f)\vec{I}_3 \\
\simeq\ &\int_{d\Omega_{back}} L(-\phi_2) r_3^2 d\Omega_{bk} \int\int L(-i_{2(3)}) \frac{P_3(\theta_3)}{4\pi r_3^2} L(-i_{1(3)}) L(-i_{2(2)}) \frac{P_2(\theta_2)}{4\pi r_2^2} L(-i_{1(2)}) \\
&\times e^{-\beta_e(r_3+r_2+z_1)} L(-\phi_2)\vec{I}_0 \beta_s^2 dV_2 dV_1. \qquad (2.50)
\end{aligned}$$

From Eq (2.27)-(2.30):

$$\varphi_3 = \varphi_2 = \varphi_1, \qquad (2.51)$$

$$\vartheta_1 = 0, \qquad (2.52)$$

$$\vartheta_3 = \pi. \qquad (2.53)$$

Inserting Eq. (2.51)-(2.53) into Eq (2.8) leads to:

$$\cos\theta_2 = \cos\vartheta_2, \qquad (2.54)$$

$$\cos\theta_3 = -\cos\vartheta_2, \qquad (2.55)$$

from which we obtain:

$$\theta_2 = \vartheta_2 = \pi - \theta_3. \qquad (2.56)$$

With Eq. (2.9) and (2.10), we obtain:

$$\lim_{\vartheta_1\to 0}\cos i_{1(2)} = \lim_{\vartheta_1\to 0}\frac{\cos\vartheta_2-\cos\theta_2\cos\vartheta_1}{\sin\theta_2\sin\vartheta_1} = \lim_{\vartheta_1\to 0}\frac{2\cos\theta_2\sin^2\frac{\vartheta_1}{2}}{2\sin\theta_2\cos\frac{\vartheta_1}{2}\cos\frac{\vartheta_1}{2}} = 0, \quad (2.57)$$

$$\cos i_{2(2)} = 1, \quad (2.58)$$

$$\cos i_{1(3)} = 1, \quad (2.59)$$

$$\lim_{\vartheta_3\to\pi}\cos i_{2(3)} = \lim_{\vartheta_3\to\pi}\frac{\cos\vartheta_2-\cos\theta_3\cos\vartheta_3}{\sin\theta_3\sin\vartheta_3} = 0. \quad (2.60)$$

Inserting Eq. (2.51)-(2.60) into Eq. (2.50), we obtain:

$$\begin{aligned}
&\int_{d\Omega_{bk}} r_{bk}^2 d\Omega_{bk} L(-\phi_f)\vec{I}_3 \\
\simeq\ &\int_{d\Omega_{bk}} \beta_s^2\frac{d\Omega_{bk}}{4\pi}\int\frac{L(-\phi_2)P_3(\pi-\theta_2)P_2(\theta_2)L(-\phi_2)}{4\pi}e^{-\tau_{bk}-\beta_e r_2}dr_2 d\Omega_2 \\
&\times\int e^{-\beta_e z_1}\vec{I}_0 dV_1 \\
\simeq\ &\frac{\beta_s^2 A}{4\pi r_3^2}\frac{1}{4\pi}\int\int L(-\phi_2)\begin{pmatrix} f_{11} & f_{12} & 0 & 0 \\ f_{12} & f_{11} & 0 & 0 \\ 0 & 0 & f_{33} & f_{34} \\ 0 & 0 & -f_{34} & f_{33}\end{pmatrix}L(-\phi_2)e^{-\beta_e r_2(1+\cos\theta_2)}dr_2 d\Omega_2 \\
&\times\begin{pmatrix}1\\1\\0\\0\end{pmatrix}\int_{z_1} e^{-2\beta_e z_1}dz_1
\end{aligned}$$

$$
\begin{aligned}
&= \frac{\beta_s^2 A}{4\pi r_3^2}\frac{1}{2}\int\int \begin{pmatrix} f_{11} & 0 & 0 & 0 \\ 0 & \frac{1}{2}(f_{11}-f_{33}) & 0 & 0 \\ 0 & 0 & -\frac{1}{2}(f_{11}-f_{33}) & 0 \\ 0 & 0 & 0 & f_{33} \end{pmatrix} e^{-\beta_e r_2(1+\cos\theta_2)} \sin\theta_2 dr_2 d\theta_2 \\
&\quad \times \begin{pmatrix} 1 \\ 1 \\ 0 \\ 0 \end{pmatrix} \int_{z_1} e^{-2\beta_e z_1} dz_1 \\
&= \frac{\beta_s^2 A}{4\pi r_3^2}\frac{1}{2}\int\int \begin{pmatrix} f_{11} \\ \frac{1}{2}(f_{11}-f_{33}) \\ 0 \\ 0 \end{pmatrix} e^{-\beta_e r_2(1+\cos\theta_2)} \sin\theta_2 dr_2 d\theta_2 \int_{z_1} e^{-2\beta_e z_1} dz_1, \qquad (2.61)
\end{aligned}
$$

where

$$
\begin{aligned}
f_{11} &= P_{11}(\pi-\theta_2)P_{11}(\theta_2) + P_{12}(\pi-\theta_2)P_{12}(\theta_2), \\
f_{12} &= P_{12}(\pi-\theta_2)P_{11}(\theta_2) + P_{11}(\pi-\theta_2)P_{12}(\theta_2), \\
f_{33} &= P_{33}(\pi-\theta_2)P_{33}(\theta_2) - P_{34}(\pi-\theta_2)P_{34}(\theta_2), \qquad (2.62) \\
f_{34} &= P_{34}(\pi-\theta_2)P_{33}(\theta_2) + P_{33}(\pi-\theta_2)P_{34}(\theta_2).
\end{aligned}
$$

We find Eq.(2.61) is exactly the same as work done by Raković and Kattawar [18] but with a different approach. Eq.(2.61) is also similar to the Eq. (4.64) in [5].

CHAPTER III

MONTE CARLO INTEGRATION AND MODEL RESULTS

A. Algorithm

Because the lidar backscatter is time dependent, there is no way to obtain the contributions from Eq. (2.44) and the second order term (2.61) analytically. Not to mention high order terms, it is very time-consuming even for the second order term if we use a regular grid to evaluate the integral. The Monte Carlo method, which randomly chooses the grid, is adopted. When considering the volume elements, they can be written in terms of four groups of variables:

$$dV_n = r_n^2 \sin\theta d\theta d\phi = r_n^2 \sin\vartheta d\vartheta d\varphi = dx_n dy_n dz_n = dx'_n dy'_n dz'_n \tag{3.1}$$

Theoretically, we can sample any group of them, (r_n, θ_n, ϕ_n), $(r_n, \vartheta_n, \varphi_n)$, (x_n, y_n, z_n), or (x'_n, y'_n, z'_n), to evaluate the integral. Generally, it is suggested that any integral that can be integrated should be done before the sampling. This will help accelerate the process and get a good expectation value. Eq. (1.27)-(1.29) are used, and we

sample $(W(r_n), P_{cumu}(\theta_n), \frac{\phi_n}{2\pi})$ instead of these four groups of variables:

$$\int_{d\Omega_{bk}} r_{bk}^2 d\Omega_{bk} L(-\phi_f)\vec{I}_{m+1}$$
$$\simeq \frac{\omega_s^m A}{4\pi r_{bk}^2}\int_m \cdots \int_1 L(-\varphi_m)P(\pi-\vartheta_m)\Big(\prod_{n=3}^{n=m} L(-i_{2(n)})\frac{P(\theta_n)}{P_{11}(\theta_n)}L(-i_{1(n)})\Big)$$
$$\times\frac{P(\theta_2)}{P_{11}(\theta_2)}e^{-\tau_{bk}}L(-\phi_2)\begin{pmatrix}1\\1\\0\\0\end{pmatrix}\Big(\prod_{n=2}^{n=m}\frac{dP_{cumu}(\theta_n)dW(r_n)d\phi_n}{2\pi}\Big)de^{-\beta_e z_1}, \qquad (3.2)$$

The main algorithm can be expressed by Fig. 6. (ϑ_1, φ_1) and $(\vartheta_{m+1}, \varphi_{m+1})$ are predetermined for the mth order contribution (see Eq. (2.27)-(2.35)). After (r_n, θ_n, ϕ_n) are sampled, other variables like (ϑ_n, φ_n), $i_{1(n)}$, $i_{2(n)}$, x'_n, y'_n and z'_n can be obtained by Eq. (2.8)-(2.9) as we did for the second order scattering. The phase matrix $P(\theta_n)$ is determined by θ_n and a pre-calculated phase matrix look up table Fig. 7. Inserting these quantities back into Eq. (3.2) and omitting $\frac{A}{4\pi r_{bk}^2}$, we obtain the power contribution from $(m+1)$th order scattering.

Generally, this process is explained in terms of photons. The path for each photon is recorded by (x'_n, y'_n, z'_n) and an integer is assigned by using a predetermined step length, Δs , to denote the range of the path length. The power contributions from photons having the same scattering order and range number will be added together. Notice that the last phase matrix $P(\pi - \vartheta_m)$ can not be reduced by an importance sampling! This method has the same problem as one may find in the discrete ordinated method when the forward peak of $P_{11}(\theta)$ is too large, which is

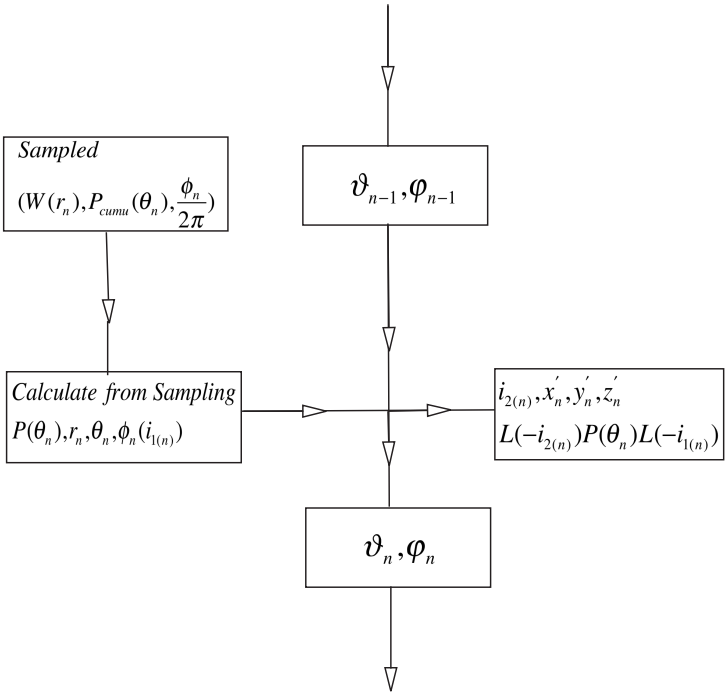

Fig. 6. Main algorithm.

generally approximated by δ approximation or Gaussian distribution [35, 36].

Phase matrixes are calculated by using codes introduced in [37, 38] with Gamma size distribution [39]:

$$n(r) = n_0 r^{(1-3v_{eff})/v_{eff}} e^{-r/r_{eff}v_{eff}}, \tag{3.3}$$

$$N = \int_0^\infty n(r)dr, \tag{3.4}$$

$$\beta_{s,a} = \int_0^\infty n(r)\sigma_{s,a}(r)dr. \tag{3.5}$$

The most commonly used unit for $n(r)$ is $cm^{-3}\mu m^{-1}$ with N denoting the number of particles per cm^3. For simplicity, the effective variance v_{eff} is set to 0.1 in calculation. The wavelength of the CALIPSO lidar is 532 nm. The refractive indice of water and ice at this wavelength are $1.33712 + i1.818 \times 10^{-9}$ [40] and $1.31167 + i1.4898 \times 10^{-9}$ [41], respectively.

Fig. 7 is the phase matrices of water cloud droplets with different effective radii:

$$P_{ij}(\theta)' = \frac{\int_0^\infty P_{ij}(\theta, r)Q_e(r)\pi r^2 n(r)dr}{\int_0^\infty Q_e(r)\pi r^2 n(r)dr}, \tag{3.6}$$

$$Q_e = \frac{\sigma_e}{\pi r^2}, \tag{3.7}$$

where Q_e and σ_e are extinction coefficiency and extinction cross section, respectively.

B. Model Results

We tested the code by attempting to create the pattern shown by Raković and Kattawar [18] under the conditions of CALIPSO lidar. We assumed a parallel plane water cloud with a thickness of 1 km. The satellite, which has a field of view of

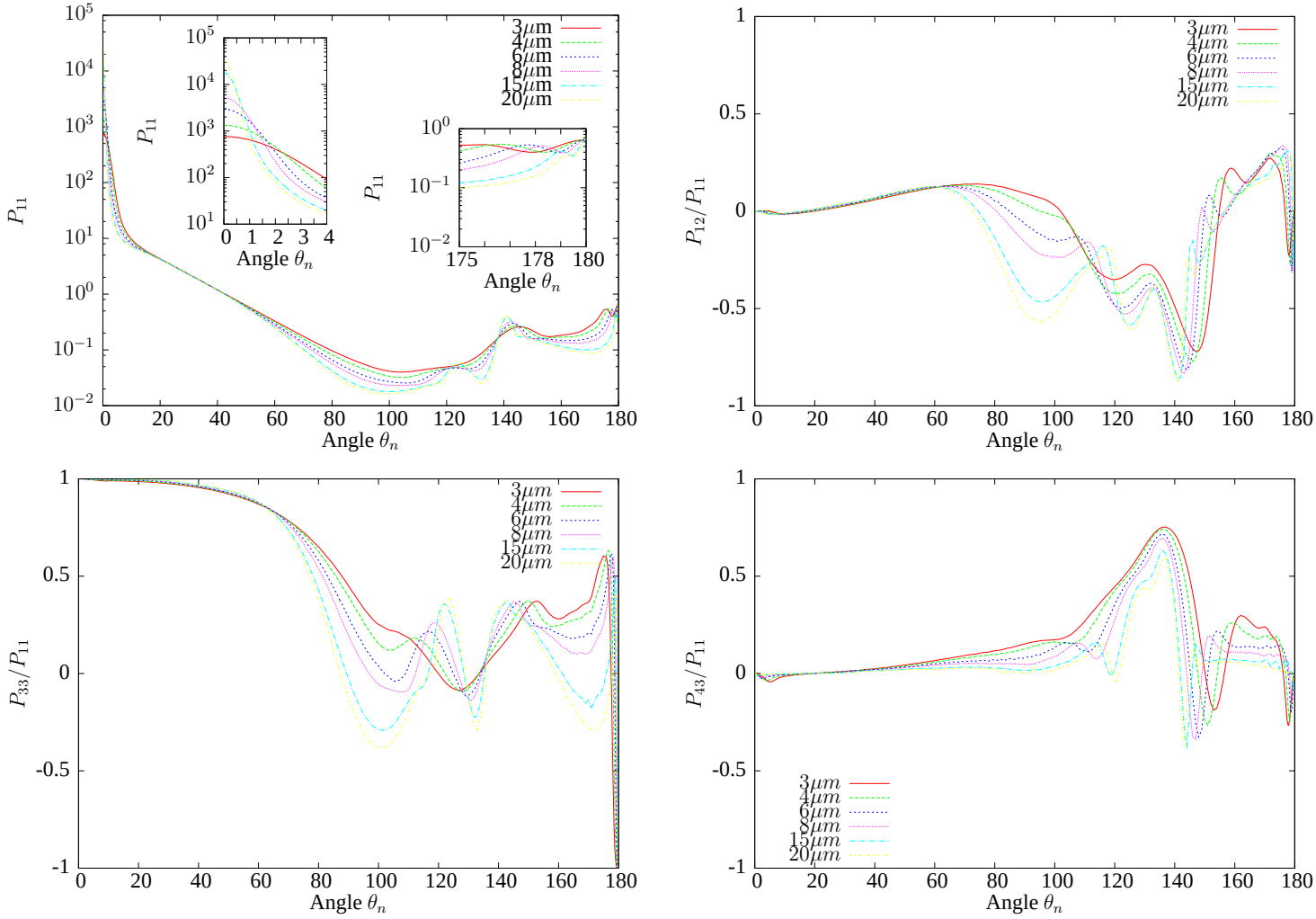

Fig. 7. Number distribution averaged phase matrices of water cloud droplets of different effective radii.

130 μrad, is 700 kms above the cloud. Patterns from different situations can be found in other papers [20, 21, 22, 23, 24]. Fig. 8 is the pattern simulated, at an optical depth of 1 in the cloud, when a delta function ray is used. Layer integrated signals also show similar patterns. However, the energy drops very quickly as it moves away from the center of the FOV with an extinction coefficient, β_e, of 13.3/km. Fig. 9 is an example of the relative strength of contributions from different orders of scattering. The data points of the first order follow the equation:

$$\frac{P_{11}(\pi)\omega_s}{2}(1 - e^{-2\beta_e \Delta s})e^{-2(i-1)\beta_e \Delta s} \tag{3.8}$$

where i is the order number of each point, i.e. a common factor of $\frac{A}{4\pi}$ is omitted for range corrected energy, $r_{back}^2 I_1$, and the emitted energy, which is $110mJ$ for the CALIPSO lidar, is assumed to be a unit. Fig. 9 illustrates that the contributions from either large order scatterings or large depth behave less smoothly than those from lower orders. This is inevitable for multidimensional definite integrals, and the case becomes worse for large size particles and better for small size particles.

Although there are numerous cases with different effective radii, extinction coefficients and total scattering orders, we focus on the following two cases:

1. Water droplets with 6 different effective radii; $3\mu m$, $4\mu m$, $6\mu m$, $8\mu m$, $15\mu m$ and $20\mu m$, and all with the same extinction coefficient, β_e, of 13/km. The first 4 orders scatterings are calculated;

2. Water droplets of 2 different effective radii, $3\mu m$ and $6\mu m$, with different extinction coefficients, β_e . The first 7 orders scatterings are calculated.

All calculations are limited to an optical depth of 4.

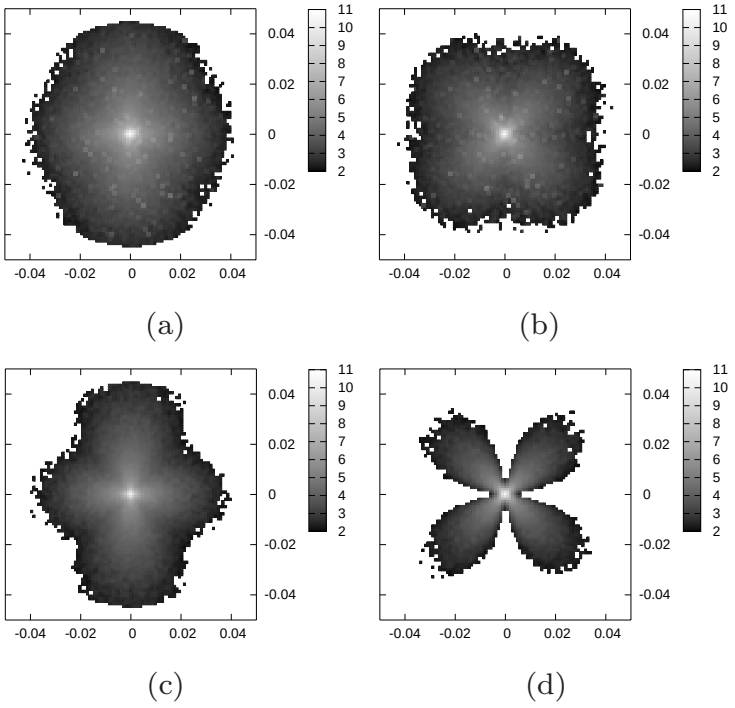

Fig. 8. Simulated range corrected signals from a cloud with $r_{eff} = 8.0\mu m$ and $\beta_{ext} = 13.3/km$ when 100 million photons are sampled. (a) and (b) are I_l and I_r, which are the sum of the first 4 order scatterings. They mainly display the patterns of the second order scattering (c) and (d). The color bar shows the intensity with the number denoting the power of the natural exponential. The idea is from Raković and Kattawar [18].

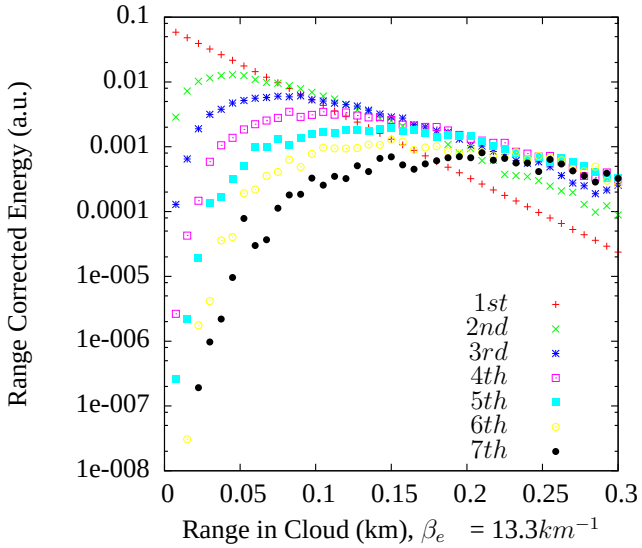

Fig. 9. Simulated range corrected signals of seven order scatterings from a cloud with $r_{eff} = 3.0\mu m$ when 10 million photons are sampled. The idea is from Winker and Poole [9].

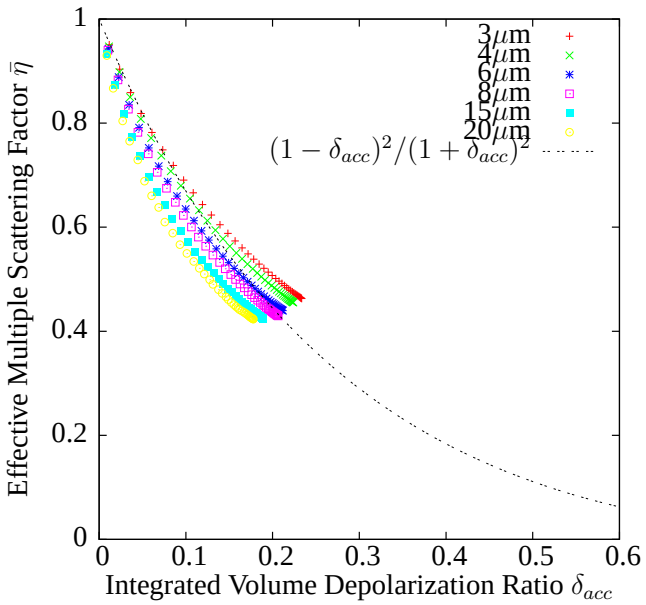

Fig. 10. Relation between effective multiple scattering factor, $\bar{\eta}$, and integrated volume depolarization ratio, δ_{acc}, of Case 1. The dashed line is from Hu et al. [26].

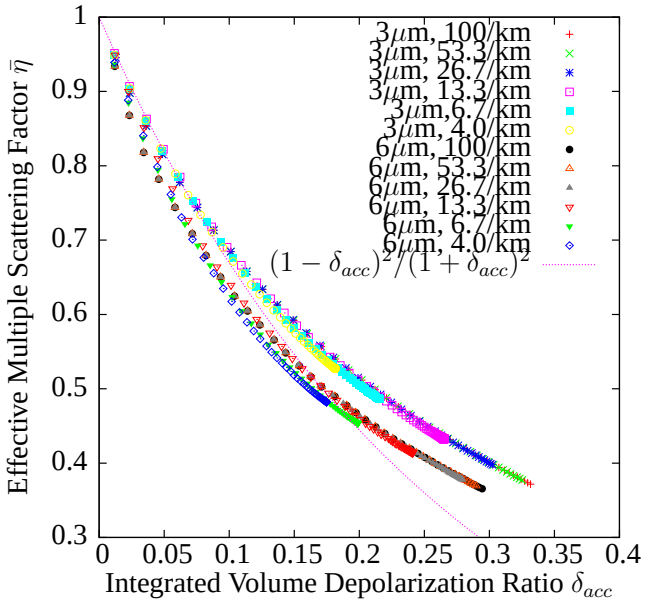

Fig. 11. Relation between effective multiple scattering factor, $\bar{\eta}$, and integrated volume depolarization ratio, δ_{acc}, of Case 2. The dashed line is from Hu et al. [26].

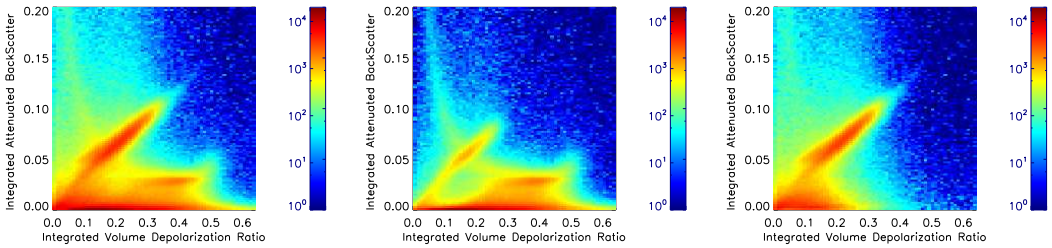

Fig. 12. Statistical summary for clouds detected by CALIPSO lidar from 15-30 November 2008. (a) the total profile of clouds, (b) the cloud with temperature below -20 $^{\circ}C$ while (c) the cloud with temperature above -20 $^{\circ}C$. The idea is after Hu et al. [27]. More figures can be found in the work of Cho et al.[43].

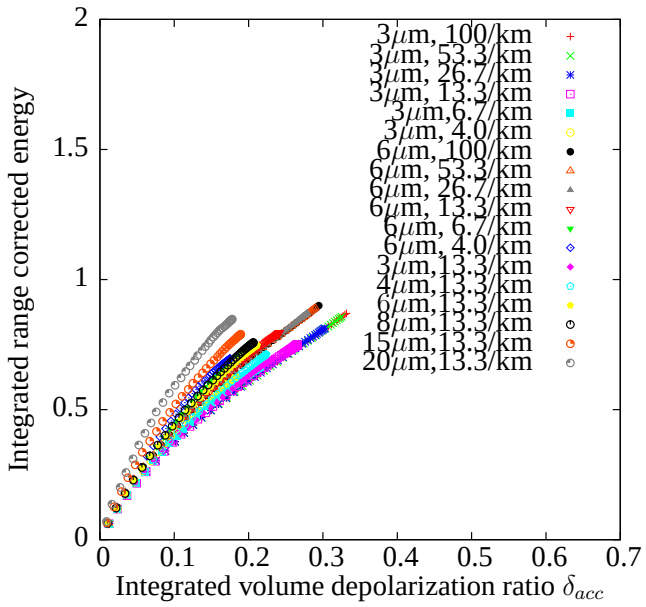

Fig. 13. Relation between integrated volume depolarization ratio, δ_{acc}, and integrated range corrected energy for both Case 1 and Case 2.

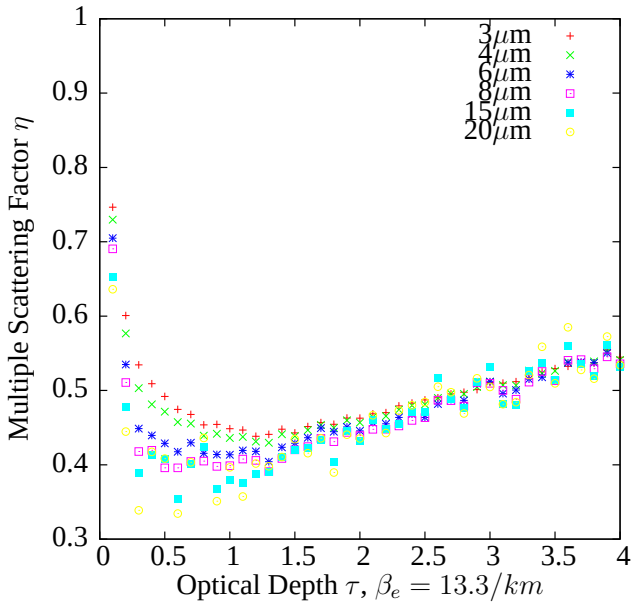

Fig. 14. Relation between multiple scattering factor, η, and optical depth, τ, of Case 1.

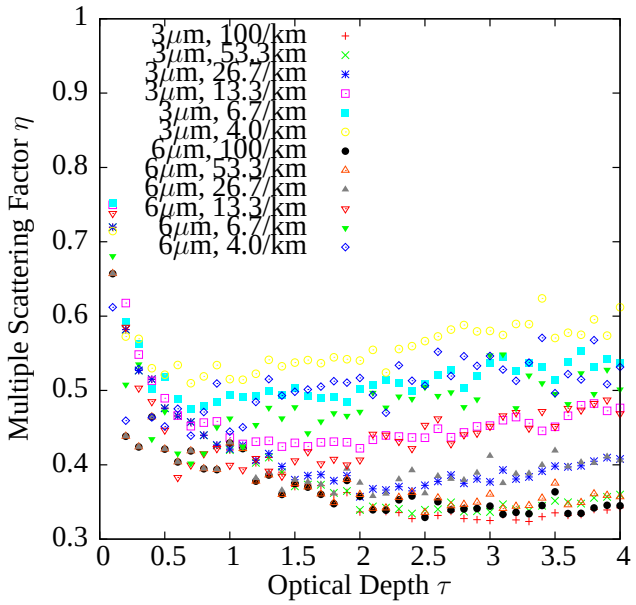

Fig. 15. Relation between multiple scattering factor, η, and optical depth, τ, of Case 2.

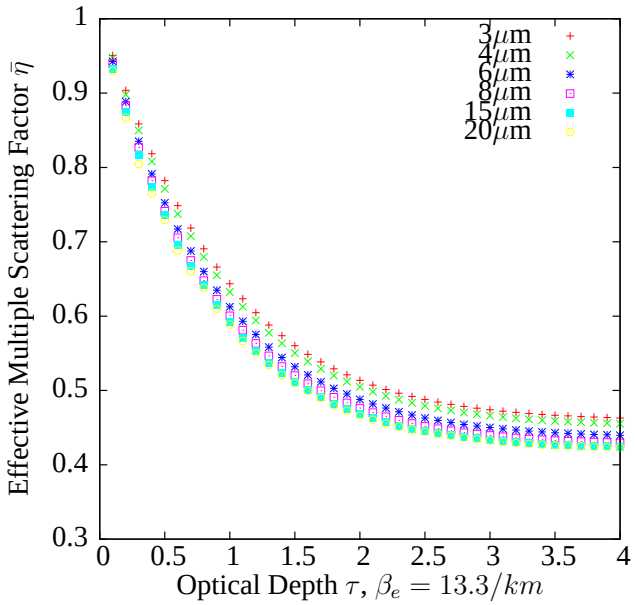

Fig. 16. Relation between effective multiple scattering factor, $\bar{\eta}$, and optical depth, τ, of Case 1.

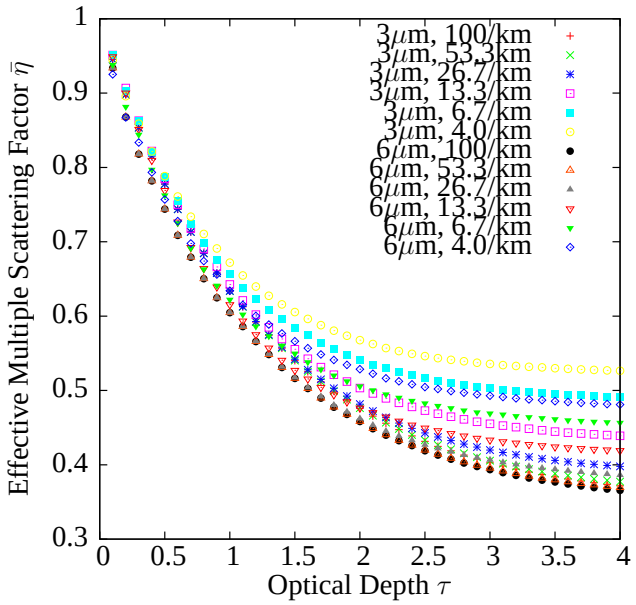

Fig. 17. Relation between effective multiple scattering factor, $\bar{\eta}$, and optical depth, τ, of Case 2.

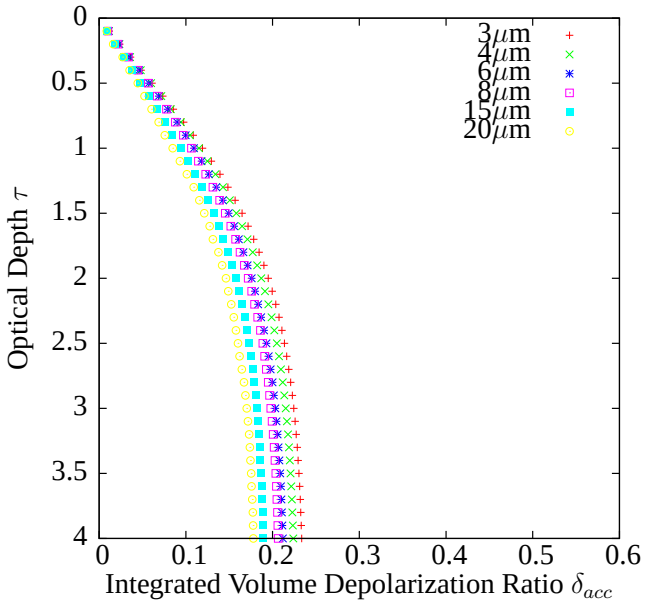

Fig. 18. Relation between integrated volume depolarization ratio, δ_{acc}, and optical depth, τ, for Case 1.

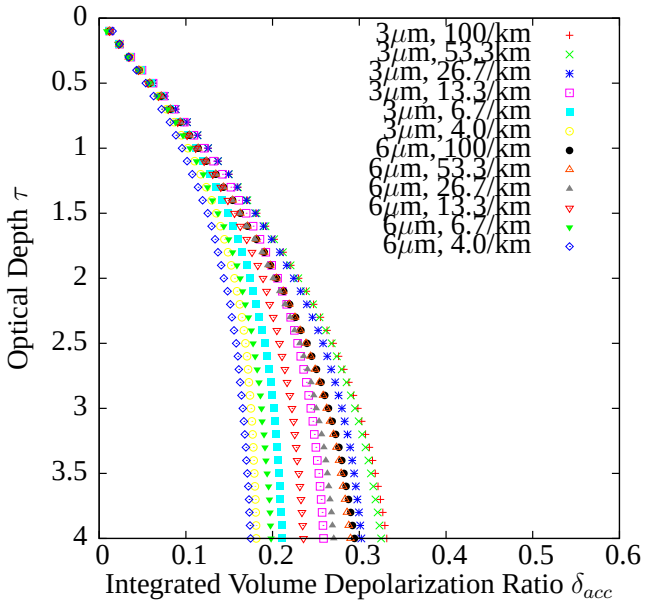

Fig. 19. Relation between integrated volume depolarization ratio, δ_{acc}, and optical depth, τ, for Case 2.

Figs. 10 and 11 show the relation between the effective multiple scattering factor, $\bar{\eta}$, and the volume integrated depolarization ratio, δ_{acc}, which are defined as follows [42, 26, 27]:

$$\bar{\eta}(z) = \frac{\int_{top}^{z} I_{single} dz'}{\int_{top}^{z} I_{total} dz'} \tag{3.9}$$

$$\delta_{acc}(z) = \frac{\int_{top}^{z} I_{total,\perp} dz'}{\int_{top}^{z} I_{total,\parallel} dz'} \tag{3.10}$$

where z is the range of cloud thickness; $I_{total}(z)$ is the intensity contribution from clouds at an altitude of z; $I_{total,\parallel}$ and $I_{total,\perp}$ are the parallel and perpendicular components. However, for multiple scattering contributions, z is defined as the length of the optical path. The relationships shown in Figs. 10 and 11 mainly follows but deviates from the work done by Hu et al. [26]:

$$\bar{\eta} = \frac{(1-\delta_{acc})^2}{(1+\delta_{acc})^2} \tag{3.11}$$

Our simulation shows that the relationship is sensitive to the effective size and the extinction coefficient of the cloud. In Figs. 10 and 11, we can see that a cloud with a larger effective size has a smaller effective multiple scattering factor, $\bar{\eta}$. A cloud with a larger extinction coefficient has a larger volume integrated depolarization ratio, δ_{acc}. Since the attenuated backscatter is proportional to the inverse of the relation [27], the integrated attenuated-backscatter, γ', from a cloud with a large effective size will be larger. Clouds with larger optical depths or extinction coefficients will have larger attenuated backscatter if the effective sizes are the same. Thus, various water clouds with different effective sizes, optical depths and extinction coefficients will lead to a water clouds pattern as shown in Fig. 12, derived from the statistics

of clouds detected from the CALIPSO lidar. Fig. 13 is the simulated results for water clouds. Although the cloud fractions and units of vertical axes can't not be confirmed, the curve is of a similar type to the diagonal parts in Fig. 12 (b). The integrated range corrected energies are obtained by:

$$r_{back}^2 \int_{top}^{z} I_{total}(z')dz' \tag{3.12}$$

Fig. 13 also shows that, under the same conditions, the integrated range corrected energy of a cloud with large effective size is larger than that of a cloud with a small effective size. A comparison between Figs. 12 and 13 shows that those pixels around the bottom left in Fig. 12 may correspond to optically thin clouds. The empirical relationship Eq. 3.11 is probably part of the story.

Figs. 14 - 17 are calculated multiple scattering factors, η, and effective multiple scattering factors, $\bar{\eta}$, in the range of clouds of Case 1 and 2, where η is [7]:

$$\eta(z) = 1 - \frac{1}{2\tau(z)} ln \frac{I_{total}(z)}{I_{single}(z)} \tag{3.13}$$

$$\tau(z) = \int_{top}^{z} \beta_e(z')dz' \tag{3.14}$$

Since there is only single scattering at $z = 0$, $\eta(0)$ and $\bar{\eta}(0)$ are equal to 1.0 theoretically. However, any measurements are made within a depth of Δs, which will lead to non-zero multiple scattering contributions from clouds ranging from $z = 0$ to $z = \Delta s$ and result in a negative start of $\eta(0)$ in Eq. (3.13), as shown in the results of Platt [7]. Since our simulated I_{single} and I_{total} are actually integrals, and will be affected by the resolution, Δs, the effective multiple scattering factor, $\bar{\eta}$, which is a ratio between two integrals, is more reliable than the multiple scattering factor,

η. In our simulation, we also found that contributions from multiple scattering will quickly surpass that from single scattering as the ray penetrates into clouds, the sink of η, as shown in Fig. 14 around small optical depth, become deep as size increase while $\bar{\eta}$ behaves more stably than η. Both η and $\bar{\eta}$ are sensitive to the extinction coefficient.

Figs. 18 and 19 show the relationship between the integrated volume-depolarization-ratio, δ_{acc}, and the optical depth, τ. With the same optical depth and extinction coefficient, a cloud with a small effective size tends to have a large δ_{acc}. To obtain a large δ_{acc}, contributions from high order scatterings are as important as second order scattering.

Fig. 20 shows the depolarization ratio, $\delta(\tau)$, for Case 2, with significant differences from δ_{acc}:

$$\delta(\tau) = \frac{I_{total,\perp}(\tau)}{I_{total,\parallel}(\tau)} \tag{3.15}$$

As we have pointed out previously, each simulated I_{total} is actually an integral over Δs , and the depolarization ratio, $\delta(\tau)$, in Fig. 20 is an approximation. In our simulation, multiple scatterings dominate at a large optical depth, τ,and photons are almost totally depolarized with an optical depth of 4. We also found $\delta(\tau)$ to be β_e sensitive, which is probably because of the light propagation in the horizontal direction. With a large β_e, more photons can be trapped in the FOV and contribute more energy to the backscatter than the case with small β_e, thus we obtain a larger $\delta(\tau)$ with a large β_e than with a small one. We also tested Case 2 with 10 million photons and found negligible difference between two groups of depolarization ratio

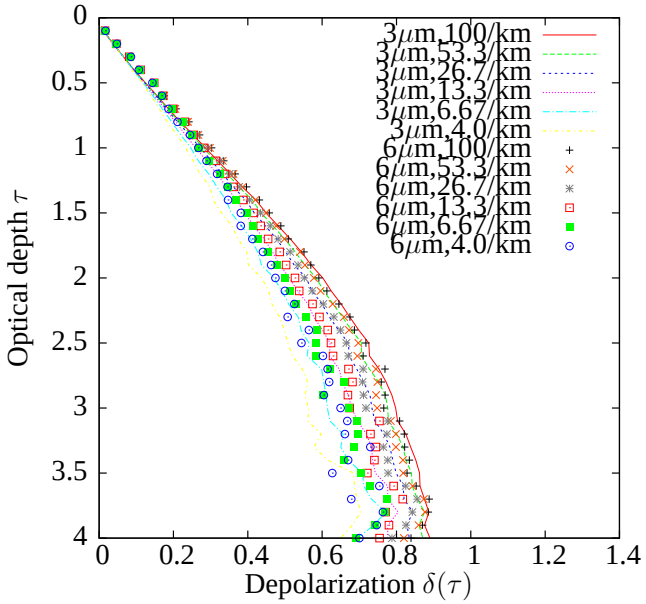

Fig. 20. Depolarization ratio profile.

when τ is less than 2. When τ becomes large, the difference become obvious. This is because the energy contribution from large optical depth is much smaller than that from small optical depth and it can be easily impacted by newly added photons. However, the results of $\delta(\tau)$ are very different from the work done by Hu et al. [25] and You et al. [31], which is probably because of the conditions used in the code.

CHAPTER IV

CONCLUSION AND FUTURE WORK

A. Conclusion

We revisited the relationship between the integrated volume depolarization ratio and effective multiple scattering factor for two cases of water clouds, using a newly developed Monte Carlo code. Our results mainly agree with the empirical relationship derived by Hu at el., and is sensitive to effective size, extinction coefficient and optical depth. The simulated results, shown in Fig 13, for integrated range-corrected-backscatter and integrated volume-depolarization-ratio are similar to the pattern displayed by a water cloud in Fig. 12 drawn from the CALIPSO lidar data. From our simulations, water clouds with relatively large effective sizes are noticed in the top right boundary of the water pattern while clouds with relatively small effective sizes show up in the lower left boundary of the pattern. Along the water pattern in Fig. 12, the extinction coefficients and optical depth of clouds increase from lower left toward the middle. Although more confirmation is needed, this could be a possible explanation of why water clouds show a pattern.

B. Future Work

As we mentioned in the introduction, there are many lidar models. These models, more or less, are related to the radiative transfer equation. The differences between them, in my opinion, are mainly in the source terms, the way the radiative transfer equation is transformed and the way the scattering phase matrices are approximated.

There may be a way to unify those models. The phase matrices of oriented particles are much more complicated than those of water droplets, and Eq. (2.39) could be used for the simulation of lidar returns from clouds consisting of oriented particles.

REFERENCES

1. K. E. Kunkel and J. A. Weiman, "Monte Carlo analysis of multiply scattered lidar return," J. Atoms. Sci. **33**, 1772-1781 (1976).

2. V. A. Kovalev and W. E. Eichinger, *Elastic Lidar: Theory, Practice, and Analysis Methods* (Wiley-Interscience, New Jersey, 2004).

3. R. T. H. Collis, "Lidar," Advances in Geophysics **13**, 113-139 (1969).

4. K. N. Liou and R. M. Schotland, "Multiple backscattering and depolarization from water clouds for pulsed lidar system," J. Atmos. Sci. **28**, 772-784 (1971).

5. E. W. Eloranta, "Calculation of doubly scattered lidar return," Ph.D. thesis (University of Wisconsin, 1972).

6. S. R. Pal and A. I. Carswell, "Polarization properties of lidar backscattering from clouds," Appl. Opt. **24** 1530-1535 (1973).

7. C. M. R. Platt, "Remote sounding of high clouds III: Monte Carlo calculation of Multiple-scattering lidar returns," J. Atmos. Sci. **38**, 156-167 (1981).

8. P. Bruscaglioni, A. Ismaelli, and G. Zaccanti, "Monte-Carlo calculations of lidar return: Procedure and results," Appl. Phys. B **60**, 325-329 (1995).

9. D. Winker and L. R. Poole, "Monte-Carlo calculations of cloud returns for ground-based and spaced-based lidars,"Appl. Phys. B **60**, 341-344 (1995).

10. U. G. Oppel, A. V. Starkov, and M. Noormohanmmadian, "A stochastic model and a variance-reduction Monte-Carlo method for the calculation of light transport,"Appl. Phys. B **60**, 335-340 (1995).

11. C. Flesia and P. Schwendimann, "Analytical multiple-scattering extention of the Mie theory: The LIDAR equation,"Appl. Phys. B **60**, 331-334 (1995).

12. L. R. Bissonnette, "Multiple scattering of narrow light beams in aerosols,"Appl. Phys. B **60**, 315-323 (1995).

13. E. P. Zege, I. L. Katsev, and I. N. Polonsky, "Analytical solution to lidar return signals from clouds with regard to multiple scattering,"Appl. Phys. B **60**, 325-353 (1995).

14. Luc R. Bissonnette, "Multiple-scattering lidar equation," Appl. Opt. **35**, 6449-6464 (1996).

15. E. W. Eloranta, "Practical model for the calculation of multiply scattered lidar returns," Appl. Opt. **37** 2464-2472 (1998).

16. L. R. Bissonnette, P. Bruscaglioni, A. Ismaelli, G. Zaccanti, A. Cohen, Y. Benayahu, M. Kleiman, S. Egert, C. Flesia, P. Schwendimann, A. V. Starkov, M. Noormohammadian, U. G. Oppel, D. M. Winker, E. P. Zege, I. L. Katsev, and I. N. Polonski, "Lidar multiple scattering from clouds," Appl. Phys. B **60**, 355-362 (1995).

17. K. N. Liou and H. Lahore, "Laser sensing of cloud composition: A backscattered depolarization technique," J. Appl. Meteorol. **13**, 257-263 (1974).

18. M. J. Raković and G. W. Kattawar, "Theoretical analysis of polarization patterns from incoherent backscattering of light," Appl. Opt. **37**, 3333-3338 (1998).

19. M. J. Raković, G. W. Kattawar, M. Mehrűbeoğlu, B. D. Cameron, L. V. Wang, S. Rastergar, and G. L. Coté. "Light backscattering polarization patterns from turbid media: Theory and experiment," Appl. Opt. **38**, 3399-3408 (1999).

20. A. I. Carswell and S. R. Pal, "Polarization anisotropy in lidar multiple scattering from clouds," Appl. Opt. **19**, 4123-4126 (1980).

21. S. R. Pal and A. I. Carswell, "Polarization anisotropy in lidar multiple scattering from atmospheric clouds," Appl. Opt. **24**, 3464-3471 (1985).

22. M. Dogariu and T. Asakura, "Polarization-dependent backscattering patterns from weakly scattering media," J. Opt. (Paris) **24**, 271-278 (1993).

23. M. Dogariu and T. Asakura, "Photon pathlength distribution from polarized backscattering in random media," Opt. Eng. **35**, 22342239 (1996).

24. G. Roy and N. Roy, "Relation between circular and linear depolarization ratios under multiple-scattering conditions," Appl. Opt. **47**, 6563-6579 (2008).

25. Y. Hu, D. Winker, P. Yang, B. Baum, L. Poole, and L. Vann, "Idenification of cloud phase from PICCASSO-CENA lidar depolarization: A multiple scattering sensitivity study," J. Quant. Spectro. Radiat. Transfer **70**, 569-579 (2001).

26. Y. X. Hu, Z. Y. Liu, D. Winker, M. Vaughan, V. Noel, L. Bissonnette, G. Roy, and M. McGill, "Simple relation between lidar multiple scattering and depolarization for water clouds," Opt. Lett. **31**, 1809-1811 (2006).

27. Y. X. Hu, M. Vaughan, Z. H. Liu, B. Lin, P. Yang, D. Flittner, B. Hunt, R. Kuehn, J. P. Huang, D. Wu, S. Rodier, K Powell, C. Trepte, and D. Winker, "The depolarization - attenuate backscatter relation: CALIPSO lidar measurements vs. theory," Opt. Express **15**, 5327-5332 (2007).

28. S. Chandrasekhar, *Radiative Transfer* (Dover, New York, 1960).

29. K. N. Liou, *An Introduction to Atmospheric Radiation* (Academic Press, San Diego, 2002).

30. J. W. Hovernier and C. V. M. Van der Mee, "A vector radiative transfer model for coupled atmosphere and ocean systems based on successive order of scattering method," Astron. Astrophys. **128**. 1-16 (1983).

31. Y. You, G. W. Kattawar, P. Yang, Y. X. Hu, and B. A. Baum, "Sensitivity of depolarized lidar signals to cloud and aerosol particle properties," J. Quant. Spectro. Radiat. Transfer **100**, 470-482 (2006).

32. M. I. Mishchenko, L. D. Travis, and A. A. Lacis, *Scattering, Absorption, and Emission of Light by Small Particles* (Cambridge, New York, 2002).

33. H.C van de Hulst, *Light Scattering by Small Particles* (Dover, New York, 1981).

34. S. Weinzierl, "Introduction to Monte Carlo methods," arXiv:hep-ph/0006269v1, (arxive.org, 2000)

35. G. E. Thomas and K. Stamnes, *Radiative Transfer in the Atmosphere and Ocean* (Cambridge, New York, 2002).

36. J. H. Joseph, W. J. Wiscombe, and J. A. Weinman, "The delta-Eddington approximation for radiative flux transfer," J. Atmos. Sci. **33**, 2452-2459 (1976).

37. W. Wiscombe, "Improved Mie scattering algorithms," Appl. Opt. **19**, 1505-1509 (1980).

38. M. I. Mishchenko and L. D. Travis, "Capabilities and limitations of a current FORTRAN implementation of the T-matrix method for randomly oriented, rotationally symmetric scatterers," J. Quant. Spectrosc. Radiat. Transfer, **60**, 309-324 (1998).

39. J. E. Hansen and L. D. Travis, "Light scattering in planetary atmospheres," Space Sci. Rev. **16**, 527-610 (1974).

40. D. Segelstein, "The Complex Refractive Index of Water," M.S. thesis (University of Missouri–Kansas City, 1981).

41. S. G. Warren and R. E. Brandt, "Optical constants of ice from the ultraviolet to the microwave: A revised compilation," J. Geophys. Res. **113**, D14220 (2008).

42. C. M. R. Platt, D. M. Winker, M. A. Vaughan, and S. D. Miller, "Backscatter-to-extincion ratios in the top layers of tropical mesoscale convective systems and in isolated cirrus from LITE observations," J. Appl. Meteor. **38**, 1330-1345 (1999).

43. H.-M. Cho, P. Yang, G. W. Kattawar, S. L. Nasiri, Y. Hu, P. Minnis, C. Tepte, and D. Winker, "Depolarization ratio and attenuated backscatter for

nine cloud types: Analyses based on collocated CALIPSO lidar and MODIS measurements," Opt. Express **16**, 3931-3948 (2008).

VITA

Name: Jianxu Lu

Address: ChanTou Village, HuangTianFan Town, DongYang, ZhangJiang, China 322102.

Email: lujianxu81@gmail.com

Education: B.S., Physics, University of Science and Technology of China, June 2004.

M.S., Physics, Texas A&M University, December 2007.

The typist for this thesis was Jianxu Lu.